Numerical simulation of viscous unsteady type IV shock-shock interaction with thermochemical nonequilibrium

Gregory H. Furumoto
California Univ., Los Angeles

Xiaolin Zhong
California Univ., Los Angeles

AIAA, Aerospace Sciences Meeting & Exhibit, 35th, Reno, NV, Jan. 6-9, 1997

Self-sustained unsteady type IV shock-shock interference heating problems with nonequilibrium real gas effects are studied by numerical simulations. The multicomponent Navier-Stokes equations with nonequilibrium rotational, vibrational, and chemical models for five-species air were solved by a finite-volume second-order TVD scheme together with a third-order semi-implicit Runge-Kutta scheme. The present paper studies the effects of impinging shock location on the unsteadiness of the nonequilibrium flow. Perfect gas cases were studied to examine the difference between perfect and nonequilibrium unsteady shock interactions. A feedback mechanism, whereby disturbances generated during the vortex shedding perturbed the main bow shock which fed back disturbances through the supersonic jet to the shear layer, was observed in the flow field. The degree of unsteadiness in the flow field was found to be strongly dependent on the location of the impinging shock relative to the geometric stagnation line. Thermochemical nonequilibrium was found to decrease surface pressure enhancement, increase surface heating enhancement, and increase the oscillation frequency relative to flow fields with identical freestreams, but without nonequilibrium models. (Author)

Numerical Simulation of Viscous Unsteady Type IV Shock-Shock Interaction with Thermochemical Nonequilibrium

Gregory H. Furumoto*, and Xiaolin Zhong†

University of California, Los Angeles, CA 90095

Abstract

Self-sustained unsteady type IV shock-shock interference heating problems with nonequilibrium real gas effects are studied by numerical simulations. The multicomponent Navier-Stokes equations with nonequilibrium rotational, vibrational, and chemical models for five-species air were solved by a finite-volume second-order TVD scheme together with a third-order semi-implicit Runge-Kutta scheme. A prior numerical study of unsteady nonequilibrium shock interactions identified a vortex shedding mechanism driving the unsteadiness. The present paper expands upon this past work to parametrically study the effects of impinging shock location the unsteadiness of the nonequilibrium flow. Perfect gas cases were studied to examine the difference between perfect and nonequilibrium unsteady shock interactions. A feedback mechanism, whereby disturbacnes generated during the vortex shedding perturbed the main bow shock which fed back disturbacnes through the supersonic jet to the shear layer, was observed in the flowfield. The degree of unsteadiness in the flowfield was found to be strongly dependent on the location of the impinging shock relative to the geometric stagnation line. Thermochemical nonequilibrium was found to decrease surface pressure enhancement,increase surface heating enhancement, and increase the oscillation frequency relative to flowfields with identical freestreams, but without nonequilibrium models.

Introduction

Understanding the flow fields around steady and maneuvering hypersonic vehicles are vital for their design. The high speeds create the possibility for many types of shock interactions near the vehicle body which can strongly affect the magnitudes of surface heating rates and skin friction. The type IV shock-shock interactions, which can occur at the engine inlet cowl lip, is of particular interest in this study. Figure 1 shows a type IV interaction which is caused by an impinging oblique shock intersecting the free stream bow shock ahead of a body. This interaction creates a transmitted shock which then impinges upon the lower bow shock (due to the flow behind the initial impinging oblique shock). Behind this transmitted shock, which is weaker than either bow shock, a supersonic jet is formed in the surrounding subsonic flow. This jet impinges on the body, ending in a terminating strong shock. At the jet impingement point, extremely high surface pressures and heating rates are encountered [1-3]. As the flow is expanded over the body surface, it once again becomes supersonic. This creates a shear layer along the body between the flow from the jet and the subsonic bulk flow behind the bow shock. This type of interaction has been shown to be inherently unsteady [4,5] in perfect gas flows.

The perfect gas type IV interaction problem has been extensively studied experimentally and analytically [2,6], and numerically [3-5]. Lind [5] performed a detailed numerical study of unsteady type IV interactions in perfect gas flows, including an examination of the effect of turbulence on the flowfield. Included in this work was a parametric study on the effect of shock impingement location on the surface loading and unsteadiness as well as the identification of the mechanism believed to account for the oscillations in the supersonic jet. It was found that vortices formed by the high velocity gradients near the jet impingement point were shed off into the bulk flow periodically. This created a periodic pressure variation near the jet impingement point, inducing oscillations in the jet. This is shown schematically in Figure 2. However, due to the high temperatures found in these interactions, real gas effects need to be

1

considered for many of these flow studies. Real gas effects have a noticeable impact on flow structure, such as the reduction of the shock stand off distance in a blunt body flow [7],and surface parameters such as surface heating rates, which can be either reduced or enhanced depending on the nature of the chemical nonequilibrium.

Because of their importance, real gas effects have recently been the focus of several studies. Steady type IV interactions were studied numerically by Prabhu, et al. [8] for equilibrium chemistry. More recently, Sanderson [9] experimentally and analytically examined the effects of nonequilibrium on the entire range of shock-shock interference flows. Unsteady phenomena in the flowfields were noted, however a detailed study of the unsteady nature of a type IV flow was outside the scope of the study. A nonequilibrium numerical study was done by Brück [10] which looked at the effects of nonequilibrium and impinging shock location on flow structure and surface pressure and heat flux. Recently, Furumoto, Zhong, and Skiba [11] began an investigation of unsteady type IV interactions with nonequilibrium real gas effects using numerical simulations. The presence of real gas effects was found to strongly affect the structure of the flow field and the degree of surface heating enhancement, relative to an undisturbed flow. Additionally, a vortex shedding process at the jet impingement point was observed to be the mechanism driving the unsteady motion of the flow. This was consistent with the findings of Lind [5] for perfect gases. The location of the shock interaction point was found to affect the degree of unsteadiness in the flow field.

The objective of the present work is to extend the study of nonequilibrium effects presented in Reference [11] for unsteady type IV shock interference heating problems. Numerical simulations are used as a tool to gain a detailed description of the unsteady flow field and to perform parametric studies of factors that may influence the fluid mechanics of the flow in the nonequilibrium regime.

Physical Model

Equations of Motion

The governing equations and pyhsical models used in this study are detailed in Reference [11] and follow those of Candler [12], Gökçen [13], Park [14],

and Gupta et al [15]. The flow is modeled by the multicomponent Navier-Stokes equations for a mixture of thermally perfect gases with the nonequilibrium rotational and vibrational energy modes modeled by separate temperatures, T_r and T_v, respectively [12,13,16]. Heat transfer is modeled using Fourier's Law for heat conduction [11]. For chemically reacting flow, multicomponent diffusion is approximately modeled by Fick's Law for binary diffusion.

Transport Coefficients

The viscosity and translational thermal conductivity models are detailed in Reference [11]. Individual species viscosities are calculated using the model of Moss [17], and mixture viscosity is computed using Wilke's mixture rule [18]. The species translational heat conduction coefficients are given by Eucken's relation [16], and the overall coefficient is then calculated using Wilke's formula in a similar fashion to the viscosity coefficient [19]. The mixture thermal conductivities for the rotational and translational modes and the diffusion coefficients, D_i, were calculated using two different models.

Transport Model 1

The first model is the original model used in Reference [11] which uses very simple formulations for the mixture thermal conductivities of the nonequilibrium modes, and the diffusion coefficient. The thermal conductivities associated with the rotational and vibrational modes are given by [13]:

$$\kappa_{(v,r)} = \sum_{i=1}^{nd} \left(\frac{\rho_i}{\rho}\right) \kappa_{(v,r)i} \qquad (1)$$

where the sums are taken over the diatomic species only and:

$$\kappa_{ri} = \mu_i R_i \qquad (2)$$

$$\kappa_{vi} = \mu_i \frac{R_i(\theta_{vi}/T_v)^2 e^{\theta_{vi}/T_v}}{(e^{\theta_{vi}/T_v} - 1)^2} \qquad (3)$$

The mass diffusion coefficient is taken to be the same for all species, $D_i = D$ and is found by assuming a constant Schmidt number [13]:

$$Sc = \frac{\mu}{\rho D} = 0.5 \qquad (4)$$

2

Transport Model 2

The second model employs curve fits and physically more rigorous formulations of the mixture values of thermal conductivities and mass diffusivities based on kinetic transport theory. A detailed description and derivation of the models can be found in Reference [15].

The nonequilibrium mixture thermal conductivities are calculated using a similar method to the translational conductivities:

$$\kappa_{(v,r)} = \sum_{i=1}^{nd} \frac{X_i \kappa_{(v,r)i}}{\sum_{j=1}^{NS} X_j \phi_{ij}} \tag{5}$$

where ϕ_{ij} is the same as those used in Wilke's mixture rule for viscosity [18].

A mixture mass diffusivity [15], $D_i = D_{im}$, between species i and the mixture is calculated by:

$$D_{im} = \frac{\sum_{j \neq i} X_j}{\sum_{j \neq i} X_j / \mathcal{D}_{ij}} \tag{6}$$

where X_j is the mole fraction of species j. Binary mass diffusivities are calculated using a curve fit [15]:

$$\mathcal{D}_{ij} = \frac{10^{-4}}{p(atm)} \exp\left((B_{Dij} \ln T_t + C_{Dij}) \ln T_t + D_{Dij}\right) \tag{7}$$

where the coefficients, $B_{Dij}, C_{Dij}, D_{Dij}$, are tabulated in Reference [15].

Comparison of Transport Models

Of the two models outlined above, Model 1 is computationally more efficient, and is therefore preferable based on cost considerations. However, Model 2 is the physically more rigorous of the two, and is therefore preferable based on the physics of the problem. The choice of models is then a trade off between cost and physical rigor. To compare the two, the values of the transport coefficients were compared under thermochemical equilibrium conditions for five species air and dissociating nitrogen, the two test gas mixtures used in this study.

Figures 3 and 4 show the total mixture thermal conductivity for air and nitrogen, respectively. Both gas mixtures were taken to be in equilibrium at a given temperature. Temperatures range from 1000 K to 10000 K. For both air and nitrogen, Model 1 and Model 2 show little difference in the value of the thermal conductivity under equilibrium conditions.

Figure 5 shows the mixture diffusion coefficients for five species air in equilibrium. Temperature ranges from 1000 K to 10000 K. The individual species mixtures diffusivities vary significantly. Additionally, none of them are very close to the constant Schmidt number value of Model 1 above 3000 K. For air flows where diffusion effects are expected to be significant and temperatures are expected to be above 3000 K, Model 2 would appear to be the preferred choice.

Figure 6 shows the mixture diffusion coefficients for dissociating nitrogen in equilibrium. Temperature ranges from 1000 K to 10000 K. Because only two species are present, the individual species diffusivities are equal to each other (*i.e.* the gas is a binary system). Additionally, Model 2 and Model 1 show good agreement up to a temperature of about 6000 K. Therefore, if the temperatures are not expected to exceed this limit over most of the flowfield, Model 1 would be adequate.

Source Terms

Chemistry is modeled using a five species model (N_2, O_2, NO, N, O). The five species reaction model is presented in Reference [11]. Two models for the rate coefficients (the k_f and k_b's) are used. The first model is the Dunn-Kang rate coefficients based on a two temperature model as presented by Häuser, et al. [20] The backward and forward coefficients are calculated using a modified Arrhenius expression of the form:

$$k = CT_x^{-\eta} exp(\theta_d / T_x) \tag{8}$$

where C, T_x, η, and θ_d for each reaction are given in Reference [20]. The second model is the Park chemistry model for air [14,21]. In this model, only the forward rate coefficients are explicitly calculated by a modified Arrhenius equation similar to that used in the Dunn-Kang model. The backward rate coefficients are then deduced from the forward rates using the equilibrium constant:

$$k_b = k_f / K_{eq} \tag{9}$$

3

The equilibrium constants are given by empirical curve fits of the form:

$$K_{eq} = \exp\left(\frac{A_1}{Z} + A_2 + A_3\ln(Z) + A_4 Z + A_5 Z^2\right) \tag{10}$$

where $Z = 10000/T$, the A_j's are presented in Refence [14], and the forward reaction rate coefficients are given in Reference [21].

The energy transfer modes considered are translation-vibration coupling, vibration-dissociation coupling, and rotation-translation coupling. Other modes were assumed to be negligible in their effect [13]. Vibration-translation and rotation-translation modes were modeled using the Landau-Teller model [16]. The vibrational relaxation time is computed using the Millikan and White formula [22] with the correction factor given by Park [14]. The rotational relaxation time is calculated using the formulation from Gökçen [13]. The model used for vibration-dissociation coupling is the one employed by Candler [12]. The derivation of this model can be found in Reference [12]. Details of these models are presented in Reference [11].

Numerical Method

The numerical method used is the same as that given in Reference [11] The inviscid fluxes were solved via a second-order finite volume TVD formulation using characteristic variable extrapolation with the Roe flux difference splitting Riemann solver [23]. Roe averaging for nonequilibrium gases followed the formulation developed by Grossman, et al. [23,24] Viscous fluxes were discretized via central differences. Time stepping was handled by the third order Additive Semi-Implicit Runge-Kutta scheme, details of which can be found in Reference [25].

Code Validation

In Reference [11], a psuedo-steady Mach reflection and a steady hypersonic flow over a cylinder were used to validate the code's time accurate and nonequilibrium capabilities. In the present paper, four additional validation cases are presented. The first case compares the Dunn-Kang and Park chemistry models. The second case compares computed surface heating with experimental data for flow over a cylinder. The third case is used as a grid refinement study. The fourth case validates the code's

ability to accurately model a type IV shock interference flow field by comparing computed results with experimental data.

Case 1: Comparison of Chemistry Models

Candler [7] showed that for cylinder flow, including chemical nonequilibrium, but with only a one temperature (thermal equilibrium) model, did a very poor job in capturing the shock standoff distance and shape, while a full thermochemical nonequilibrium model produced accurate results. To validate the nonequilibrium capability of the code and to test two different chemistry models, hypervelocity flow past cylinders based on published experimental data was computed. Hornung [26] studied flow past a 1 inch diameter cylinder with $u_\infty = 5590\ m/s$, $T_\infty = 1833°K$, $p_\infty = 2910\ Pa$ and a Reynolds number of 6000. The gas in the freestream was partially dissociated nitrogen, 92.7% N_2 and 7.3% N by mass. The flow conditions match those studied experimentally by Hornung and computationally by Candler [7]. Two chemistry models were used for this case to test their effectiveness in the simulation of reacting hypersonic flows. The first model was the Dunn-Kang rate coefficient model [20], and the second model was the Park model [14]. Calculation were performed on 80 × 80 grids with exponential stretching in the body normal direction. A sample grid is shown in Figure 7.

Figure 8 compares computational results using the Dunn-Kang model, shown in the bottom half of the figure, to an experimental interferogram published by Hornung [26,27], shown in the top half of the figure. The computational shock shape and standoff distances agrees very well with the experimental data. Slight differences between the interference fringe shapes of the computation and experiment are visible.

Figure 9 compares computational results using the Park model, shown in the bottom half of the figure, to an experimental interferogram published by Hornung [26,27], shown in the top half of the figure. Once again, the computed shock shape and standoff distance are in good agreement with experiment. As before, small differences between the interference fringe shape of the computation and experiment exist. These differences are mainly along the stagnation line.

4

American Institute of Aeronautics and Astronautics

As a comparison between the two chemistry models, Figure 10 presents fringe number profiles along the stagnation line for both models along with experimental data taken from Reference [26]. The profiles show that both models tended to yield results closer to an equilibrium solution than demonstrated by experiment, while the Park model solutions were closer to experiment than the Dunn-Kang solutions. While the Park model produced better results than the Dunn-Kang model, the present study primarily uses the Dunn-Kang model because it is computationally more efficient [28]. The reason for this is that the backward rate coefficients for the Dunn-Kang model has a lower operation count in terms of multiplies, divides, and logarithm and exponential evaluations than does the Park model. For example, a typical backward rate coefficient for the Dunn-Kang model has the form:

$$k_b = CT_t^{1.5} \tag{11}$$

while a typical backward rate coefficient for the Park requires evaluation of the exponential term in Equation (10).

Case 2: Comparison of Surface Heating with Experiment

Sanderson [9] studied flow past a 4.06 centimeter diameter cylinder with $u_\infty = 4450 \ m/s$, $\rho_\infty = 0.0155 kg/m^3$, $p_\infty = 5480 \ Pa$. The gas in the freestream was partially dissociated nitrogen, 99.034% N_2 and 0.966% N by mass. Calculations were carried out using the multicomponent Navier-Stokes with the Dunn-Kang chemistry model. The grid used was similar to the one described for the previous case (shown in Figure 7) with a grid szie of 192×122.

Figure 11 presents surface heating rates, represented in nondimensional form by the Stanton number $(\dot{q}/\rho_\infty u_\infty h_{o\infty})$ normalized by the theoretical stagnation point Stanton number for the given flow conditions. The figure presents both the computational results and Sanderson's experimental measurements. The vertical bars on the experimental data points represent the bounds of the experimental error presented in Reference [9]. Good agreement between experiment and computation was obtained.

Grid	$\dfrac{\dot{q}}{\rho_\infty u_\infty (H_o - H_w)}$	$\dfrac{2(p-p_\infty)}{\rho_\infty u_\infty^2}$
48×30	7.156×10^{-3}	1.822
96×60	9.522×10^{-3}	1.823
192×120	1.003×10^{-2}	1.825

Table 1: Results of grid refinement study for flow over a cylinder.

Case 3: Estimate of Numerical Error

A steady cylindrical blunt body case based on an experiment by Holden [29] was used to estimate the numerical error of the scheme used. The conditions for this case were $M_\infty = 8.033$, $T_\infty = 124.89 \ K$, and $Re_D = 3.74 \times 10^5$. The cylinder had a diameter of $0.0762 \ m$ and the freestream was undissociated nitrogen. At the given freestream temperature, the flow enthalpy is low enough such that real gas effects were not expected. Results from computations using the code with nonequilibrium real gas effects models indicate that the these effects were indeed negligible for this particular flow.

Computations were carried out on grids of three different sizes and the stagnation point heating rates presented as Stanton numbers, and pressures, presented as pressure coefficients, were compared for each grid. The results are presented in Table 1. Using the Richardson extrapolation technique [30] to estimate the error on the finest grid results in an estimate of 0.37% for the relative error in pressure. A similar analysis produces a result of 1.7% for the relative error in the numerical solution of the 192×120 grid. Because surface heating rates are viscous effects dependent on gradients near the wall, they are more sensitive than pressure to grid spacing normal to the surface and are slower to converge as the grid is refined. Figure 12 compares the surface pressure coefficients for the computational results on the 192×120 grid and experimental results. Figures 13 compares the surface heating rates for the computational results on the 192×120 grid and experimental results. The computed and experimental pressure coefficients are in good agreement. The surface heating rate is in reasonably good agreement with experiment and is slightly under predicted.

5

Case 4: Unsteady Type IV Interaction

The focus of this study is on shock interaction flows, particularly the type IV shock/shock interference heating problem, such as the one shown schematically in Figure 1. Therefore, a simulation corresponding to an experimental type IV case was computed to test the ability of the code to model such complex flows. Experiments for type IV interference flow were performed by Holden, Moselle, and Lee [29]. These experiments have become a common test case for validating numerical results of shock interaction flows [3,5,31,32]. The experimental conditions were for a 3 inch diameter cylinder in a Mach 8.03 flow. The freestream had the following conditions: $p_\infty = 985.015\ Pa$, $\gamma_\infty = 1.4$, $T_\infty = 111.56\ K$, and $T_{wall} = 294.44\ K$. The flow deflection due to the impinging shock was 12°. This flow has been found to be inherently unsteady by both experimental [2] and numerical [3,32] studies.

Computations were carried out on two grids, one a 96 × 60 grid, and the other a 192 × 120 grid. A sample grid is shown in Figure 14. Time accurate simulations were carried out using the Navier-Stokes code with SIRK time stepping and nonequilibrium real gas models. Due to the low enthalpy of the above freestream, real gas effects were expected and observed to be negligible in the computed results. As discussed in the Introduction, the type IV interference flowfield is inherently unsteady. Calculations were therefore carried out until numerical transients died out and a nondecaying limit cycle was reached.

Figure 15 presents a comparison of the time averaged pressure coefficient $(C_p = (p - p_\infty)/\frac{1}{2}\rho_\infty u_\infty^2)$ along the body surface with experimental data given in Reference [29]. Very good agreement between the computed and experimental results was obtained.

Figure 16 shows a series of computed instantaneous nondimensional surface heating rate profiles $(St = \dot{q}/\rho_\infty u_\infty(H_o - H_w))$ compared with experimental data from Reference [29]. Fair agreement between computation and experiment was obtained. The computations tended to underpredict the peak value of the surface heating. This result is consistent with other numerical studies of type IV flows [31,32]. One of the possible reasons for this may be that the grid used was unable to adequately resolve the boundary layer.

As previously mentioned, there is an inherent un-

Cylinder Radius:	0.0381 m
Flow Deflection: (impinging shock)	12°
Re:	2.57354×10^5
M_∞:	8.03
P_∞:	985.015 Pa
T_∞:	800° K
T_{wall}:	1000° K

Table 2: Flow conditions for type IV shock interaction with nonequilibrium real gas effects.

steadiness in type IV shock interactions. This inherent unsteadiness of type IV shock interactions has been previously noted by both numerical [3,32] and experimental [2,9] studies. A dominant oscillation frequency, nondimensionalized as a Strouhal number $Sh = fD/u_\infty$, was observed for the surface pressure. For perfect gas flows, numerical studies have reported a Strouhal number associated with the time variation of peak surface pressure of 1.3 [32]. Experimental results associated with the pressure variation at a fixed point on the body surface report a Strouhal number range of 0.13 to 0.45 [9]. A spectral analysis of the peak surface pressure and the pressure at a fixed point near the jet impingement point was performed. The numerical results produced a dominant nondimensional frequency of 1.3 for the peak surface pressure, and 0.185 and 1.12 for the fixed surface points. These results are consistent with both existing numerical [3,32] and experimental results [2,9] for perfect gas flows.

Unsteady Type IV Shock Interference Heating with Real Gas Effects

A two-dimensional type IV interference heating problem with real gas and unsteady effects was studied by computing two dimensional Navier-Stokes solutions and analytic modeling. The type IV shock interaction has been observed to be inherently unsteady [2,3,5,32]. The flow conditions are the same as those used in Reference [11]. The freestream was an undissociated N_2 flow and the flow conditions are given in Table 2. Under these conditions, the impinging shock wave is weak enough so that the flow behind it could still be taken as an undissociated gas in thermal equilibrium. Runs were conducted using 192 × 122 stretched grids, such as the one shown in Figure 14.

6

Case	θ_{imp}
PG-1:	$-4.16°$
PG-2:	$-4.65°$
PG-3:	$-6.19°$
PG-4:	$-8.94°$
PG-5:	$-10.5°$

Table 3: The five different shock impingement locations for the perfect gas model.

Case	θ_{imp}
NE-1:	$-3.19°$
NE-2:	$-4.84°$
NE-3:	$-6.94°$
NE-4:	$-8.83°$
NE-5:	$-11.2°$

Table 4: The five different shock impingement locations for the nonequilibrium gas model.

The computations were initiated by setting freestream conditions throughout the computational domain. The impinging shock was added by imposing the flow conditions behind the impinging shock at an appropriate location at the inflow boundary. To capture the inherent unsteady nature of the flow, the computations were run until a sustained oscillation in the maximum surface pressure was obtained to ensure all initial numerical transients had died out. The numerical results were first checked against an analytical model that used simplified equilibrium shock relations. The real gas effects and the effects of varying the impinging shock location were then numerically investigated via two dimensional unsteady simulations. A representative instantaneous contour plot of translational temperature is presented in Figure 17 to illustrate the main flow structures in a type IV interaction flow.

In order to evaluate the effects of nonequilibrium, five different impinging shock locations for both a perfect (nonreacting) and nonequilibrium gas were used in the simulations of the type IV shock interference heating problem. The shock impinging location is defined by the angular displacement of the incident shock-bow shock- transmitted shock triple point (θ_{imp})from the negative y-axis. Positive angular displacement is in the clockwise direction. The same angular coordinate system is used for surface position (θ) when surface parameters are plotted. This coordinate system is shown schematically in Figure 18. The five locations for the perfect gas (PG) model are summarized in Table 3. The five locations for the nonequilibrium gas (NE) model are summarized in Table 4.

Flowfield Analysis of Shock/Shock Interaction

As a check on the results of the numerical simulations, the computational results were compared with analytical predictions for flow variables in thermo-chemical equilibrium behind the interacting shocks. The analytic procedure used here was similar to that used by Sanderson [9]. The flow field was divided into seven zones as shown in Figure 19. In the figure, zone 1 is the freestream, zone 2 is the flow behind the impinging shock, zone 3 is the area behind the upper bow shock, zone 4 is the jet region behind the shock transmitted due to the oblique shock impingement, zone 5 is the region behind the embedded jet shock, zone 6 is the region behind the lower bow shock, and zone 7 is the region behind the terminating jet shock. The analysis is based on the shock jump conditions with the equilibrium chemistry model of Lighthill [33]. The hydrodynamic jump relations are : across oblique shocks

$$p_b - p_a = \rho_a u_a^2 \sin^2(\beta_b) \left(1 - \frac{\rho_a}{\rho_b}\right) \qquad (12)$$

$$\rho_a u_a \sin(\beta_b) = \rho_b u_b \sin(\beta_b - \delta_b) \qquad (13)$$

$$h_a + \frac{1}{2}u_a^2 \sin^2(\beta_b) = h_b + \frac{1}{2}u_b^2 \sin^2(\beta_b - \delta_b) \qquad (14)$$

$$u_a \cos(\beta_b) = u_b \cos(\beta_b - \delta_b) \qquad (15)$$

across normal shocks

$$p_a + \rho_a u_a^2 = p_b + \rho_b u_b^2 \qquad (16)$$

$$\rho_a u_a = \rho_b u_b \qquad (17)$$

$$h_a + \frac{1}{2}u_a^2 = h_b + \frac{1}{2}u_b^2 \qquad (18)$$

where subscript a denotes the incident or upstream state and subscript b indicates the post-shock downstream state. These realtions are used together with the equation of state

$$p = \rho(1 + \alpha)R_{N_2}T \qquad (19)$$

7

In the above equations, the β's are the angles the shocks make with the incident streams, and the δ's are the flow deflections with respect to the incident streams. This is shown schematically in Figure 19. The terminating jet shock separating zones 5 and 7 is assumed to be a normal shock. R_{N_2} is the gas constant for nitrogen, α is the mass fraction of atomic nitrogen in the region indicated by the subscript. The enthalpy for all zones, h, can be expressed as

$$h = \frac{7}{2}R_{N_2}T + \frac{\theta_v R_{N_2}}{exp(\theta_v/T) - 1}$$
$$+\alpha\left(\frac{3}{2}R_{N_2}T - \frac{\theta_v R_{N_2}}{exp(\theta_v/T) - 1} + h_N^o\right) \qquad (20)$$

where h_N^o is the heat of formation of atomic nitrogen.

Zones 1,2, and 4 were assumed to be chemically frozen with $\alpha = 0$, while zones 3, 5, 6, and 7 were assumed to be in thermo-chemical equilibrium governed by the Lighthill ideal dissociating gas model [33]:

$$\frac{\alpha^2}{1-\alpha} = \frac{\rho}{\rho_d}e^{-\theta_d/T} \qquad (21)$$

where θ_d and ρ_d are parameters characterizing the dissociation reaction presented by Lighthill [33], and can be found in Vincenti and Kruger [16] as $\theta_d = 113,100\ K$ and $\rho_d = 130\ g/cm^3$ for nitrogen.

To close the above system of equations, conditions of pressure and flow direction continuity across the shear layers separating zones 3 and 4 and zones 5 and 6 were used. These can be expressed as:

$$p_3 = p_4 \qquad (22)$$

$$\delta_3 = \delta_4 + \delta_3 \qquad (23)$$

$$p_5 = p_6 \qquad (24)$$

$$\delta_6 = \delta_4 + \delta_5 = \delta_3 + \delta_5 - \delta_2 \qquad (25)$$

The flow properties in zones 2 through 7 can then be found by simultaneously solving Equations (12) to (25) for the jumps across each shock in Figure 19.

Analytic Flowfield Results Compared with Numerical Simulations

The results from the analysis in the preceding sections were compared to the numerically computed flowfield for case NE-3 listed in Table 4. These numerical results were obtained from a two dimensional simulation of the Navier-Stokes equations with the nonequilibrium model. Figure 20 shows instantaneous temperature contours obtained from numerical simulations, for case NE-3. The three streamlines in the figure indicate the lines along which the computed results were extracted for comparison with the results of the analytical method. Streamline (a) passes through zones 1 and 3. Streamline (b) passes through zones 2, 4, and 5. Streamline (c) passes through zones 2 and 6 (see Figure 19).

Figure 21 shows a comparison of numerical and analytic solutions for pressure along the three streamlines in Figure 20. In the numerical simulations, nonequilibrium effects produce a finite relaxation region behind the bow shocks, evident in the temperature contours, while the analysis assumed equilibrium flow, or no relaxation region. Despite this, the computed solution and the analysis show good agreement in zone 3 (Figure 21-a), zone 4 (Figure 21-b), and zone 6 (Figure 21-c). Zone 5 shows noticeable discrepancy. This is due to the fact that in the computations, the jet is curved in this region, and therefore departs from the idealized configuration assumed in the analysis. Overall, the numerical results agree very well with the analytical method for the prediction of pressure fields in the presence of real gas effects.

Figure 22 shows a comparison of numerical and analytic solutions for temperature along the three streamlines in Figure 20. The computed solution shows all three temperatures (translational, rotational, and vibrational), while the analytic solution, being an equilibrium solution, shows only a single temperature. Note that in all computed results, the translational and rotational temperatures are essentially in equilibrium. Zones 3 (Figure 22-a) and 6 (Figure 22-c) show good agreement between computation and analysis downstream of a relaxation region just behind the shock. Zones 4 and 5 (Figure 22-b) shows significant discrepancy due to the high degree of nonequilibrium in the jet. The computed translational-rotational temperature is significantly higher than the temperature predicted by analysis. However, the computed vibrational mode is nearly frozen, as evidenced by the low vibrational temperature. Because of this, most of the internal energy in the computed flow is distributed in the translational and rotational modes. The analytic model assumed full thermal equilibrium for the internal modes. Therefore the internal energy

8

is spread among more modes. This results in the computed translational-rotational temperature being higher than the analytic temperature.

Surface Heating Analysis

Once the flowfield has been determined, the stagnation point heating rate can be estimated. Stagnation point surface heating on a blunt body for a reacting gas can be calculated using the theory of Fay and Riddell [34]. When applied to a type IV flow, the terminating jet shock is assumed to be a normal shock locally parallel to the surface of the body. Sanderson [9] used this method to derive an expression for the heating enhancement ratio ($\dot{q}/\dot{q}_{undisturbed}$) in a type IV flow [9] based on flow parameters from a flowfield analysis similar to the one given previously. The expression derived is:

$$\frac{\dot{q}_{type\ IV}}{\dot{q}_{cyl}} = 0.5099 \sqrt{\frac{D}{\Delta x}} \left(\frac{u_5^2}{u_\infty^2}\right)^{0.63} \left(\frac{\rho_5}{\rho_\infty}\right)^{0.5}$$
$$\times \left(\frac{1+\alpha_e}{1+\alpha_7}\right)^{0.28} \left(\frac{\rho_5 \rho_e}{\rho_7 \rho_\infty}\right)^{0.13} \left(\frac{h_0 + 0.2\alpha_7 h^\circ}{h_0 + 0.2\alpha_e h^\circ}\right) \quad (26)$$

The non-zero numerical subscripts refer to the regions in Fig. 19. The subscript e refers to the equilibrium solution behind a normal shock, which corresponds to the post shock solution along the stagnation streamline in undisturbed flow. h_0 is the total enthalpy, a conserved quantity. $\frac{D}{\Delta x}$ is the ratio of body diameter to jet width. This can be determined from an expression based on empirical correlations and detailed in Reference [9]:

$$\frac{\Delta x}{D} = 0.193 \exp(4.67/M_\infty^2) \frac{\rho_{fr}}{\rho_{eq}} \sin(|\beta_4 + \delta_2 - \delta_3|) \quad (27)$$

where $\frac{\rho_{fr}}{\rho_{eq}}$ is the ratio of post shock densities for a perfect gas solution (ρ_{fr}) and an equilibrium gas solution (ρ_{eq}).

The analytical results of the surface peak heating enhancement were compared to the time-averaged peak heating enhancement from the numerical simulations. The analysis predicted a surface heating enhancement rate ratio of 16.2. This is in reasonable agreement with the computed value of 17.0 for case NE-3 from the numerical simulations. In case NE-3, the terminating jet shock was locally parallel to

the surface, which was an assumption of the heating model. The differences may be due to the simplifying assumptions made in the analytical model, and differences in the real gas effects models between the analysis and simulations.

Effects of Impinging Shock Location

First, the effect of impinging shock location on the stability of the type IV interference flowfield and the surface heating and pressure loads associated with the supersonic jet impingement are examined. Cases using both the perfect gas and nonequilibrium gas models were computed. The shock locations studied are summarized in Tables 3 and 4. The results for the perfect gas model are presented first.

Perfect Gas Model

Instantaneous temperature contours of each perfect gas case are shown in Figure 23, and corresponding stream line patterns are given in Figure 24. Figure 23-a corresponds to case PG-1, Figure 23-b to case PG-2, Figure 23-c to case PG-3, Figure 23-d to case PG-4, and Figure 23-e to case PG-5 in Table 3.

From the temperature contours in Figure 23, it can be seen that the thickness of the upper body shear layer decreases as the impinging shock location is lowered. As a result, the standoff distance of the upper bow shock decreases from Figures 23-a to 23-e. Also, the orientation of the jet relative to the body changes as the impinging shock location is lowered. In Figure 23-a, the jet curves upwards, and the terminating jet shock is not parallel to the surface, whereas in Figures 23-b, -c, and -d, the termination jet shock is nearly parallel to the surface. The flow in Figure 23-e is noticeably different from the others. It has the thinnest upper body shear layer and the thickest lower body shear layer. Additionally, the upper jet boundary shear layer is almost attached to the surface near the jet impingement point.

In the streamlines of Figures 24-a through -d, the stagnation streamline lies within the supersonic jet. However, in Figure 24-e, the stagnation streamline is nearly coincident with the upper jet boundary. When this happens, the flow transitions from a type IV to a type III shock-shock interaction characterized by an upper jet boundary shear layer that attaches to the body. Also of note are the vortical

9

formations near the jet impingement point in Figures 24-b and 24-d. These formations are linked to the self sustained oscillations of the supersonic jet.

Figure 25 shows time averaged surface heating rate profiles normalized by the undisturbed stagnation point heat transfer rate. The peak heating enhancement starts at about 10.6 for case PG-1, increases to a peak of 12.2 for case PG-2, and then steadily decreases to 10.4 for case PG-4 until it suddenly increases again to 11.6 for case PG-5. Figure 26 shows time averaged pressure profiles normalized by the undisturbed stagnation point pressure. As with the surface heating, the peak pressure enhancement increases from case PG-1 to PG-2, reaches a peak, and then decreases until case PG-4. This is followed by a sudden increase for case PG-5.

The peak heating enhancement occurs at about $\theta = -15.7°$ while the peak pressure enhancement occurs at about $\theta = -22.6°$. A numerical study by Thareja, et al. [31] for a perfect gas flow indicated a pressure peak at $\theta = -22.6°$, and a heating rate peak somewhere between $\theta = -21.7°$ and $\theta = -34.2°$. While the current perfect gas cases PG-1 through PG-4 agree with the trends obtained by Reference [31], the results for PG-5 show a departure from these trends. A numerical study done by Brück [10] obtained a similar result for a perfect gas model where the peak heating and pressure enhance both peak near $\theta = -40°$ after a decreasing trend. One possible explanation for this comes from the jet geometry in case PG-5.

The supersonic jet in case PG-5 exhibits the least amount of curvature of all five cases. Compare the streamlines in Figure 24-e with Figures 24-a through -d. Case PG-5, therefore, has the weakest embedded shock of the five cases. Additionally, the jet does not terminate normal to the surface, and the terminating jet shock is not a normal shock. Because the stagnation streamlines passes through weaker shocks in case PG-5 than in cases PG-1 through PG-4, there is a smaller loss of total pressure in case PG-5, resulting in a higher stagnation point pressure.

Figure 27 presents the time histories of maximum surface pressure normalized by undisturbed stagnation pressure for the five impinging shock locations using the perfect gas model. The results show that case PG-5 was the most stable, exhibiting very little oscillation. Case PG-1 was the most oscillatory, exhibiting the largest fluctuations of all the cases.

Nonequilibrium Gas Model

The effects of impinging shock location with a nonequilibrium model are examined. Instantaneous temperature contours of each nonequilibrium gas case are shown in Figure 28, and corresponding stream line patterns are given in Figure 29. Figure 28-a corresponds to case NE-1, Figure 28-b to case NE-2, Figure 28-c to case NE-3, Figure 28-d to case NE-4, and Figure 28-e to case NE-5 in Table 4.

In case NE-1, the translational temperature contours in Figure 28-a show that the supersonic jet curves upward over the body and does not end in a terminating jet shock and directly impinge on the body. This grazing jet pattern is referred to as a type IVa interaction in Reference [6]. The structure near the cylinder surface just below the jet shown in the streamlines of Figure 29-a is a separation region created due to the fact that the stagnation streamline lies below the jet. The separation bubble formed between the stagnation point, and the jet impingement point, two regions of locally high pressure.

While the jet in Figure 28-b (case NE-2) curves upwards along the body in a similar way to the type IVa interactions, a terminating jet shock can be seen near the jet impingement point. As seen in Figure 29-b, the stagnation streamline does not reside outside and below the jet, marking this pattern as a type IV and not a type IVa flow. Jet oscillations, however, can push this flow into a type IVa pattern over part of its oscillation cycle.

For case NE-3, the translational temperature contours in Figure 28-c show the jet directly impinging on the body. Vortices are formed near the jet-wall juncture due to high velocity gradients in the regions of severe turning as shown in the streamlines of Figure 29-c. The time varying motion of these vortices is described in detail below in the discussion of the unsteady mechanism of the flow. This case also exhibited the largest range of variation for pressure surface heating enhancement.

In case NE-4, the jet in Figure 28-d directly impinges upon the body as with case NE-3 in Figure 28-c. This case also exhibits similar vortical structures to case NE-3 in the streamlines of Figure 29-d. While case NE-4 did not exhibit as large oscillations as case NE-3, it was second to that case in it's degree of unsteadiness.

10

In case NE-5, the flow shown in the translational temperature contours of Figure 28-e has a very short supersonic jet and is nearly a type III interaction. However, the stagnation streamline is coincident with the jet, as seen in Figure 29-e, unlike case PG-5 in Figure 24-e. The lower jet boundary of this flow was relatively stable, while the upper jet boundary exhibited an oscillatory nature.

Compared to the perfect gas results of Figure 23 the nonequilibrium results in Figure 28 exhibit smaller bow shock standoff distances and thinner wall shear layers. Also, the flow with real gas effects have thinner supersonic jets than their perfect gas analogs. Relative to the perfect gas streamlines in Figure 24, the nonequilibrium results in Figure 29 exhibit a much more vortical structure.

Figure 30 shows time averaged surface heat transfer profiles normalized by the undisturbed stagnation point heat transfer rate. The highest heating was produced by case NE-3, when the jet was normal to the body surface, and the lowest by the case NE-1, because of the absence of direct shock impingement on the body for case NE-1. These results are in qualitative agreement with the heating rate results obtained by Brück [10] and also reflect the trends with regards to jet impingement location reported in References [6] and [31].

Figure 31 shows time averaged pressure profiles normalized by the undisturbed stagnation point pressure. The highest peak pressure was produced by case NE-5, and the lowest by the case NE-1, because of the absence of direct shock impingement on the body for case NE-1. The reason that case NE-5 has the highest peak pressure can be inferred by examining the contours and streamlines in Figures 28 and 29. The stagnation line flow in case NE-5 only passes through two shocks, the transmitted shock and the terminating jet shock. Additionally, the terminating jet shock in case NE-5 is not a strong normal shock (compare Figures 28-e and 29-e). The stagnation lines in the other non-type IVa cases all have to pass through the transmitted shock, the embedded jet shock, and a strong terminating jet shock. The total pressure loss in case NE-5 is thus lower than in cases NE-2, NE-3, and NE-4, causing case NE-5 to have the highest stagnation point pressure.

Figure 32 presents the time histories of maximum surface pressure normalized by undisturbed stagnation pressure for the five impinging shock locations using the nonequilibrium model. The result show

Case	Average	Min.	Max.
PG-1:	10.6	7.04	18.0
PG-2:	12.2	9.10	19.4
PG-3:	10.9	10.2	16.1
PG-4:	10.4	8.93	15.6
PG-5:	11.6	10.8	14.8

Table 5: Time averaged and minimum and maximum surface heating enhancement for the perfect gas model.

that case NE-1 was the most stable, exhibiting very little oscillation. Cases NE-3 and NE-4 were the most oscillatory with case NE-3 exhibiting the highest degree of oscillation.

Comparison of Perfect Gas and Nonequilibrium Gas Results

Nonequilibrium real gas effects have a significant impact on the structure of the type IV interaction flow fields, realtive to the perfect gas flows. The bow shock standoff distances are greatly reduced for the nonequilibrium flow realtive to the perfect gas flow. The thickness of the wall shear layers are also greatly decreased. These effects can be seen in Figures 23 and 28. The nonequilibrium flows exhibit a more vortical structure than do the perfect gas flows, as seen in Figures 24 and 29. Because of this, the nonequilibrium flows are more oscillatory in nature, with larger ranges of temporal variation of peak surface pressure in Figure 32 than in the perfect gas cases in Figure 27.

The time averaged peak surface heating ratio along with the minimum and maximum peak values over the time span sampled for the perfect gas cases are summarized in Table 5 for the perfect gas cases and in Table 4 for the nonequilibrium cases.
Figure 33 presents the time averaged peak surface heating enhancement ratios for five different impinging shock locations and both the perfect gas and nonequilibrium gas models. The actual values of the wall heating enhancement are comparable between the perfect gas and the nonequilibrium results, with the perfect gas model giving values slightly below that for the nonequilibrium gas cases. The effects of chemical reactions on wall heating are expected to be more significant if catalytic walls were taken into account.

11

Case	Average	Min.	Max.
NE-1:	3.26	2.46	5.28
NE-2:	9.22	3.17	17.5
NE-3:	17.0	8.66	31.7
NE-4:	13.3	10.4	31.8
NE-5:	11.7	9.73	25.9

Table 6: Time averaged and minimum and maximum surface heating enhancement for the nonequilibrium gas model.

As mentioned previously, comparison of the time histories in Figures 27 and 32 indicate that the nonequilibrium flow exhibits a wider range of variation than does the the perfect gas flow, and that cases PG-1, and NE-3 were the two most oscillatory cases. A spectral analysis of the maximum surface pressure was used to determine the dominant frequencies in the flows. The frequencies were nondimensionalized as Strouhal numbers ($Sh = fD/u_\infty$). The dominant frequency for the perfect gas case corresponded to a Strouhal number of 1.2. The dominant frequency for the case with nonequilibrium real gas effects corresponded to a Strouhal number of 2.7. The nonequilibrium case oscillates at a much higher frequency that does the perfect gas case. The Strouhal number of the perfect gas case matches the results of past research using numerical methods [32].

The high value associated with the nonequilibrium case is unexpected as relaxation effects are expected to behave diffusively. The higher frequency may be due to the addition of short time scales related to the nonequilibrium relaxation phenomena and the shortening of the length scales due the decrease in shock standoff distance and shear layer thickness.

Unsteady Mechanism

Several researchers [3,32,35] have observed disturbances propagating from the shear layer toward the bow shock across the subsonic region of the flow. To examine disturbance trajectories in present computations, $x - t$ diagrams along three radial cuts, one through the upper bow shock, one approximately through the jet, one through the lower bow shock, are plotted for pressure fluctuation normalized by the time averaged pressure distribution. $x - t$ diagrams are presented in Figure 34 for case PG-1 and Figure 35 for case NE-3. In each plot the upper figure illustrates the three cuts along which the $x - t$ traces are made. Time has been nondimensionalized as tU_∞/R_{cyl}, where R_{cyl} is the cylinder radius.

In Figure 34-a, which is a cut through the upper bow shock, disturbances propagate primarily from the body towards the bow shock, causing disturbances in the bow shock. A similar situation occurs in the lower bow shock as seen in Figure 34-c. In Figure 34-b disturbances propagate from the transmitted shock through the jet to the wall. Similarly, for case NE-3, in Figure 35-a disturbances propagate primarily from the body towards the bow shock, inducing disturbances in the bow shock. In Figure 35-b, disturbances travel back through the jet. In Figure 35-c, disturbances propagate in both directions, however the magnitudes of the disturbances propagating from the body to the bow shock dominate over the disturbances propagating in the other direction. Disturbances from the shear layers near the body propagate towards the bow shocks. These perturbations disturb the bow shocks, causing oscillations which then affect the shock triple points and the transmitted shock. This creates perturbation waves within the jet which are convected back to the body and disturb the shear layer. This is similar to the feedback mechanism observed in the past [3,32,35].

The nonequilibrium cases exhibited a higher oscillation frequency than did the perfect gas case due to the shorter length and time scales in the nonequilibrium case. This can be seen by comparing the spacing in time of the disturbance waves in Figure 34 for the perfect gas, and Figure 35 for the nonequilibrium real gas. The waves in the nonequilibrium case are packed closer together than in the perfect gas case. The shorter length scales for the nonequilibrium gas can be seen by comparing the shock standoff distances in Figures 34-a and 35-a. The standoff distance, nondimensionalized by the cylinder radius, is about 1.0 for the perfect gas and 0.55 for the flow with nonequilibrium real gas effects.

Since case NE-3 displayed the most oscillatory nature of all the real gas effects cases studied, a detailed look at the time history of this case was done. A segment of the time history of the maximum surface pressure of case NE-3 is shown in Figure 36. The labels on the curve correspond to the time references used in the discussion that follows. Both instantaneous and time averaged surface heating profiles are presented in Figure 37. The instantaneous profiles are plotted at times corresponding to the time references in Figure 36. The profiles are normalized by

12

the undisturbed stagnation point heating rate. The surface heating profiles vary widely about the time averaged profile, reaching peak values nearly twice that of the time averaged peak heating.

Both instantaneous and time averaged surface pressure profiles are presented in Figure 38. The instantaneous profiles are plotted at times corresponding to the time references in Figure 36. The profiles are normalized by the undisturbed stagnation point pressure. Similar behavior exists between the normalized pressure profiles in Figure 38 and the normalized surface heating profiles in Figure 37. The variation of pressure and surface heating are synchronized. That is they both reach maxima and minima at the same point in the cycle. For example, at time T5, both pressure, in Figure 38 and surface heating, in Figure 37, are at their peak values, while they both reach minimal values at time T3.

Figures 39 to 41 present instantaneous translational temperature contours for case NE-3. In Figure 39, corresponding to time T1, the jet impingement location is marked J, while the points labeled A and B track disturbance waves in the flow field. The jet is nearly normal to the body surface and the surface pressure is at a local maximum as seen in Figure 36. In Figure 40, corresponding to time T3, the jet, J, has reached a nearly type IVa configuration. This point corresponds to the minimum pressure point in Figure 36 and the smallest surface heating peak in Figure 37. Disturbance A continues to move towards the bow shock, while disturbance B moves along the jet towards the body. Compression wave, C, is convected along the wall inside the shear layer. In Figure 41,the jet, J, is once again nearly normal to the wall. This point corresponds to the pressure peak in Figure 36 at time T5, and to the maximum surface heating peak in Figure 37. Disturbance A has entered the relaxation zone behind the upper bow shock, and disturbance B is strongly interacting with the supersonic jet. The compression wave, C, has been convected off through the shear layer.

Conclusions

The nonequilibrium real gas effects in a two-dimensional, high enthalpy type IV shock/shock interference heating problem have been numerically studied. Additionally, the effects of five different impinging shock locations across the type IV shock interaction have been examined. The results show

that:

1. The shock impingement location strongly affects the stability of the flowfield and the peak surface heating and pressure. Large heating rates and surface pressures are generated when the terminating normal jet shock is nearly parallel to the body, resulting in a nearly normal jet impingement.

2. Nonequilibrium real gas effects increase the dominant oscillation frequency when flow is inherently unsteady. Real gas effects reduce the macroscopic length scales by reducing shock standoff distance and wall shear layer thickness. The relaxation phenomena introduce additional small time scales to the flow.

3. For the cases studied, nonequilibrium real gas effects reduce the magnitude of the peak surface heating enhancement relative to the perfect gas flows for isothermal, noncatalytic walls.

4. A feedback mechanism was observed whereby disturbance waves are created near the jet impingement point and propagate through the subsonic region to the bow shocks. The disturbed bow shocks create perturbations in the the supersonic jet. These perturbations feed back through the jet, inducing jet oscillations, which continue the unsteadiness.

Acknowledgements

References

[1] A. R. Wieting and M. S. Holden. Experimental Shock Wave Interference Heating on a Cylinder at Mach 6 and 8. *AIAA Journal*, 27:1557–1565, 1989.

[2] M. S. Holden. *Shock-Shock Boundary Layer Interaction.* AGARD Rept. No. 764, July 1989.

[3] X. Zhong. Application of Essentially Nonoscillatory Schemes to Unsteady Hypersonic Shock-

13

Shock Interference Heating Problems. *AIAA Journal*, 32:1606–1616, 1994.

[4] G. Gaitonde and J. S. Shang. *The Performance of Flux-Split Algorithms in High-Speed Viscous Flows.* AIAA Paper 92-0186, 1992.

[5] C. A. Lind. *A Computational Analysis of the Unsteady Phenomena Associated with a Hypersonic Type IV Shock Interaction.* PhD thesis, University of Maryland, 1994.

[6] J. W. Keyes and F. D. Hains. *Analytical and Experimental Studies of Shock Interference Heating in Hypersonic Flows.* NASA TN D-7139, 1973.

[7] G. V. Candler. *On the Computation of Shock Shapes in Nonequilibrium Hypersonic Flows.* AIAA Paper 89-0312, 1989.

[8] R. K. Prabhu, J. R. Stewart, and R. R. Thareja. *Shock Interference Studies on a Circular Cylinder at Mach 16.* AIAA Paper 90-0606, 1990.

[9] S. R. Sanderson. *Shock Wave Interaction in Hypervelocity Flow.* PhD thesis, California Institute of Technology, 1995.

[10] S. Brück. *Investigation of Shock-Shock Interactions in Hypersonic Reentry Flows.* Presented at the 20th International Symposium on Shock Waves, 1995.

[11] G. H. Furumoto, X. Zhong, and J. C. Skiba. *Unsteady Shock-Wave Reflection and Interaction in Viscous Flows with Thermal and Chemical Nonequilibrium.* AIAA Paper 96-0107, 1996.

[12] G. V. Candler. *The Computation of Weakly Ionized Hypersonic Flows in Thermo-Chemical Nonequilibrium.* PhD thesis, Stanford University, 1988.

[13] T. Gökçen. *The Computation of Hypersonic Low Density Flows with Thermochemical Nonequilibrium.* PhD thesis, Stanford University, 1989.

[14] C. Park. *Nonequilibrium Hypersonic Aerothermodynamics.* Wiley Interscience, 1990.

[15] R.N. Gupta, J. M. Yos, R. A. Thompson, and K. P. Lee. *A Review of Reaction Rates and Thermodynamic Transport Properties for an 11-Species Air Model for Chemical and Thermal Nonequilibrium Calculations to 30000K.* NASA RP-1232, 1990.

[16] W. G. Vincenti and C. H. Kruger. *Introduction to Physical Gas Dynamics.* John Wiley and Sons, Inc., 1965.

[17] J. N. Moss, G. A. Bird, and V. K. Dorga. *Nonequilibrium Thermal Radiation for an Aerospace Flight Experiment Vehicle.* AIAA Paper 88-0081, 1988.

[18] C. R. Wilke. A Viscosity Equation for Gas Mixtures. *Journal of Chemical Physics*, 18(4):517–519, 1950.

[19] J. D. Anderson Jr. *Hypersonic and High Temperature Gas Dynamics.* McGraw-Hill, Inc., 1989.

[20] J. Häuser, J. Muylaret, H. Wong, and W. Berry. Computational Aerothermodynamics for 2D and 3D Space Vehicles. In T. K. S. Murthy, editor, *Computational Methods in Hypersonic Aerodynamics.* Kluwer Academic Publishers, 1991.

[21] C. Park. Review of Chemical-Kinetic Problems of Future NASA Missions, I: Earth Entries. *Journal of Thermophysics and Heat Transfer*, 7:385–398, 1993.

[22] R. C. Millikan and D. R. White. Systematics of Vibrational Relaxation. *Journal of Chemical Physics*, 12:3209–3213, 1963.

[23] B. Grossman and P. Cinella. Flux Split Algorithms for Hypersonic Flows. In T. K. S. Murthy, editor, *Computational Methods in Hypersonic Aerodynamics.* Kluwer Academic Publishers, 1991.

[24] B. Grossman and P. Cinella. Flux Split Algorithms with Non-Equilibrium Chemistry and Vibrational Relaxation. *Journal of Computational Physics*, 88:131–168, 1990.

[25] X. Zhong. *New High-Order Semi-Implicit Runge-Kutta Schemes for Computing Transient Nonequilibrium Hypersonic Flow.* AIAA Paper 95-2007, 1995.

[26] H. G. Hornung. Non-equilibrium Dissociating Nitrogen Flow Over Spheres and Circular Cylinders. *Journal of Fluid Mechanics*, 53:149–176, 1972.

[27] H. Hornung. Experimental Simulation of High-Enthalpy Real-Gas Effects. In J. A. Desideri, R. Glowinski, and J. Periaux, editors, *Hypersonic Flows for Reentry Problems, Volume 1.* Springer-Verlag, 1991.

14

[28] S. Shahpar, A. Kennaugh, I. M. Hall, and D. I. A. Poll. Comparison of Computation and Experiment for a High Enthalpy, Heated-Driver, Shock-Tube Environment. In *Theoretical and Experimental Methods in Hypersonic Flows*. AGARD-CP-514, 1993.

[29] M. S. Holden, J. R. Moselle, and J. Lee. *Studies of Aerothermal Loads Generated in Regions of Shock/Shock Interaction in Hypersonic Flow*. NASA CR-181893, October 1991.

[30] K. E. Atkinson. *An Introduction to Numerical Analysis*. John Wiley and Sons, 1989.

[31] R. R. Thareja, J. R. Stewart, O. Hassan, K. Morgan, and J. Peraire. A Point Implicit Unstructured Grid Solver for the Euler and Navier-Stokes Equations. *International Journal for Numerical Methods in Fluids*, 9:405–425, 1989.

[32] D. Gaitonde and J. S. Shang. On the Structure of an Unsteady Type IV Interaction at Mach 8. *Computers and Fluids*, 24:469–485, 1995.

[33] M. J. Lighthill. Dynamics of a Dissociated Gas Part I: Equilibrium Flow. *Journal of Fluid Mechanics*, 2:1–32, 1956.

[34] J. A. Fay and F. R. Riddell. Theory of Stagnation Point Heat Transfer in Dissociated Air. *Journal of the Aeronautical Sciences*, 25:73–85, 1958.

[35] S. Yamamoto and S. Kano. *Sturcture of Bow Shock and Compression Wave Interactions in Unsteady Hypersonic Shock/Shock Interference Flow*. AIAA Paper 96-2152, 1996.

15

American Institute of Aeronautics and Astronautics
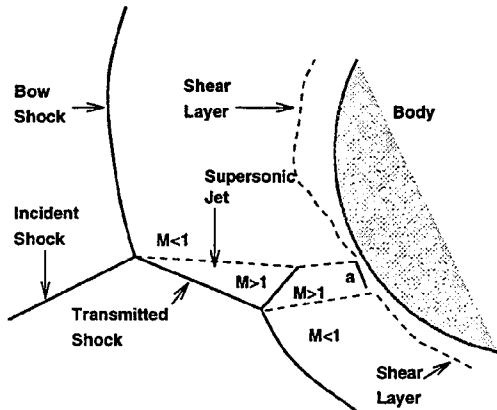
Figure 1: Schematic of type IV shock interference heating

Figure 2: Schematic of the vortex shedding mechanism responsible for the unsteadiness of the flow. The vortices are shed out of phase with respect to each other. The arrows indicate the motions of the flow structures.

Figure 3: Comparison of thermal conductivity models for a five species air model in equilibrium.

Figure 4: Comparison of thermal conductivity models in an equilibrium mixture of N_2 and N.

Figure 5: Comparison of diffusion coefficient models for a five species air model in equilibrium.
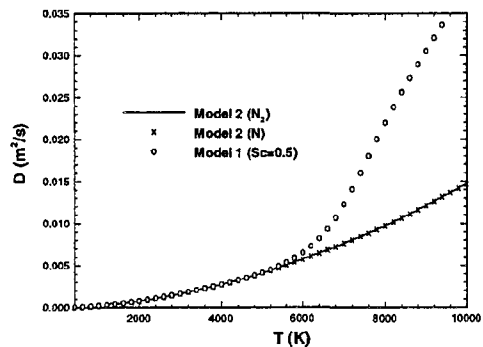
Figure 6: Comparison of diffusion coefficient models in an equilibrium mixture of N_2 and N.

16

American Institute of Aeronautics and Astronautics

Figure 7: Sample grid from the cylinder flow calculations. For clarity, the grid shown is coarser than the actual grid used.

Figure 9: Computational interferogram using the Park model (bottom) compared with experimental results of Hornung (top) for hypervelocity flow over a cylinder.

Figure 8: Computational interferogram using the Dunn-Kang model (bottom) compared with experimental results of Hornung (top) for hypervelocity flow over a cylinder.
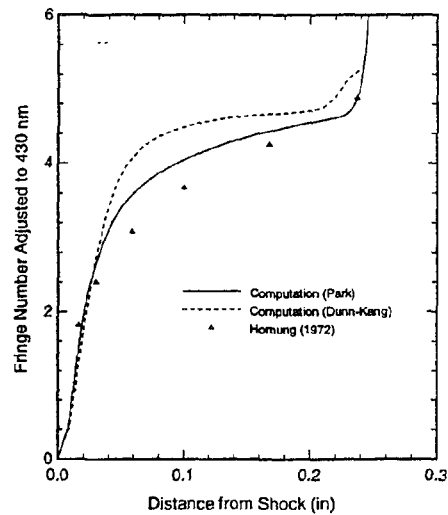
Figure 10: Computed fringe numbers for the two chemistry models compared with experimental values of Hornung along the stagnation line.

17

American Institute of Aeronautics and Astronautics
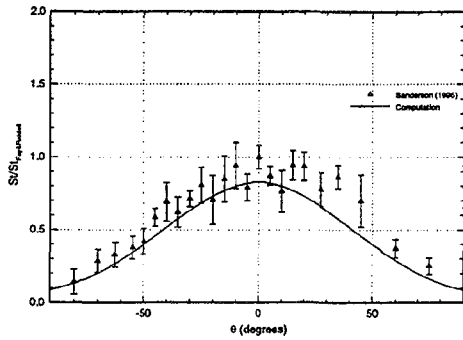
Figure 11: Computed surface Stanton number ($St = \frac{\dot{q}}{\rho_\infty u_\infty h_{o\infty}}$) profiles compared with experimental data of Sanderson.
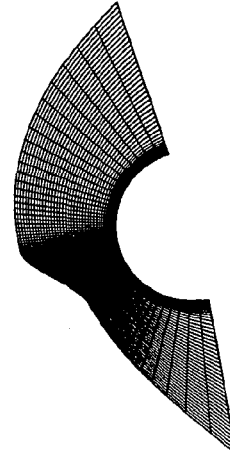
Figure 14: Sample grid used in Type IV shock interference computations. The grid is shown coarser than actual for clarity.
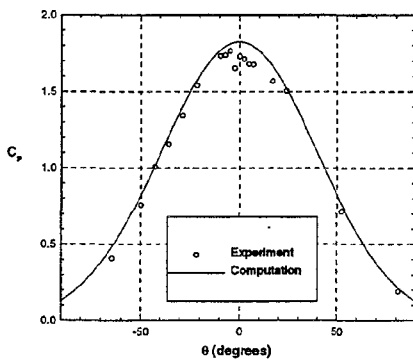
Figure 12: Computed surface pressure coefficient ($C_p = (p - p_\infty)/\frac{1}{2}\rho_\infty u_\infty^2$) profiles compared with experimental data of Holden.
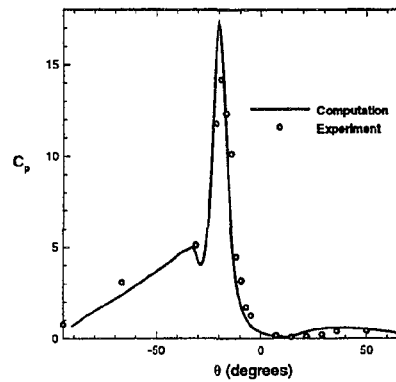
Figure 15: Computed surface pressure coefficient ($C_p = (p - p_\infty)/\frac{1}{2}\rho_\infty u_\infty^2$) profiles compared with experimental data of Holden.
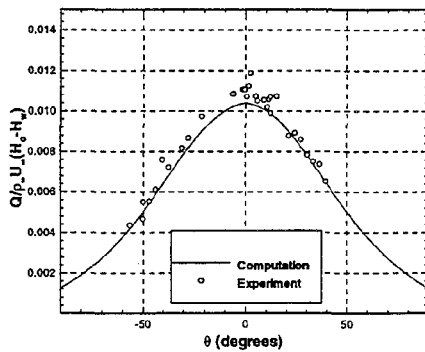
Figure 13: Computed instantaneous surface Stanton number ($St = (\dot{q}/\rho_\infty u_\infty (H_o - H_w))$) profiles compared with experimental data of Holden.
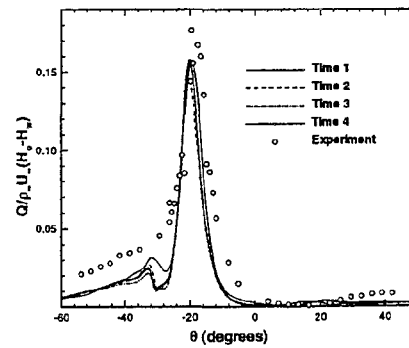
Figure 16: Computed instantaneous surface Stanton number ($St = (\dot{q}/\rho_\infty u_\infty (H_o - H_w))$) profiles compared with experimental data of Holden.

18

American Institute of Aeronautics and Astronautics
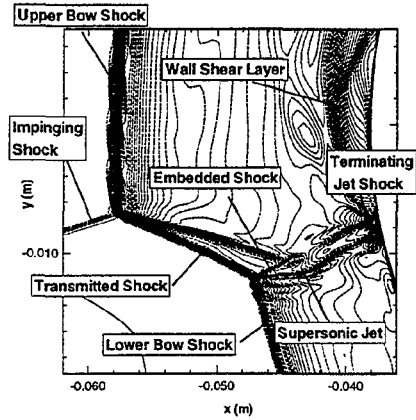
Figure 17: Type IV temperature contours illustrating the important flow structures such as the embedded shock, the supersonic jet, the shear layer along the body surface, and the terminating jet shock. Although these contours are for the nonequilibrium model, the same structures exist in the perfect gas flows.
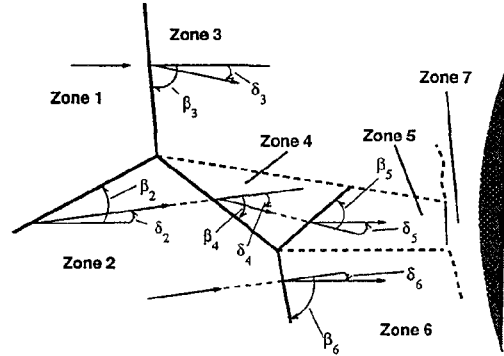
Figure 19: Schematic to illustrate zone definitions used in the analytic solution.
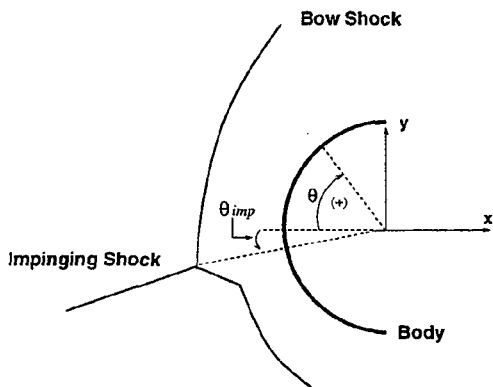
Figure 18: Definition of θ_{imp} and θ for type IV simulations.
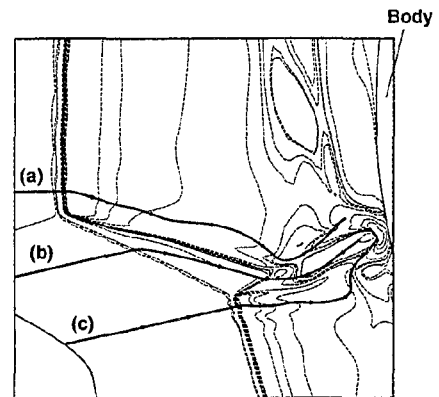
Figure 20: Type IV temperature contours illustrating the streamlines along which the computational results were plotted for comparison with analytic results.

19
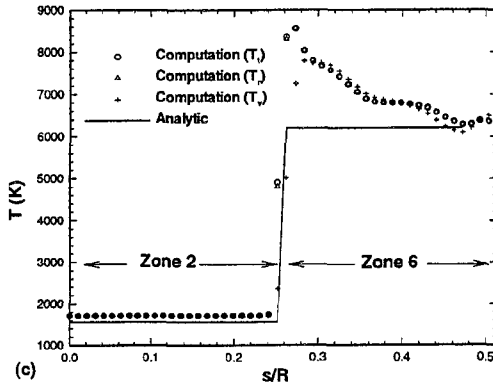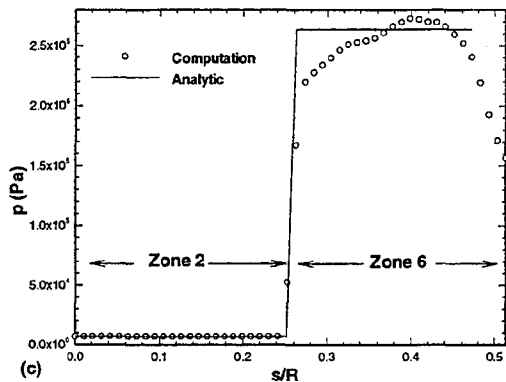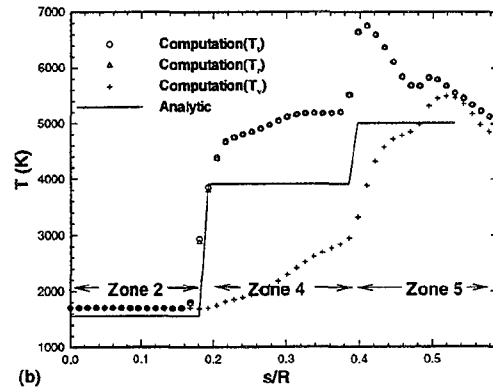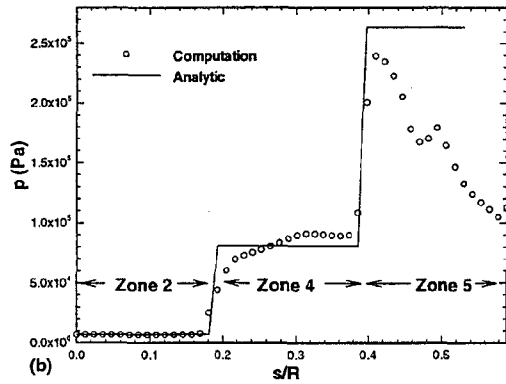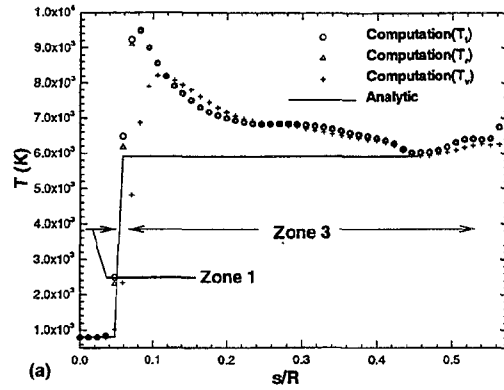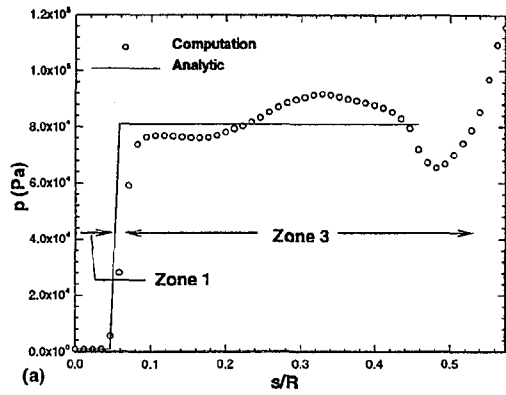
Figure 21: Comparison of numerical and analytical results for pressure (Pa). Lines indicate analytic solutions and symbols indicate results from flowfield computations. Figure labels correspond to streamlines in Figure 20: (a) streamline a, (b) streamline b, (c) streamline c.

Figure 22: Comparison of numerical and analytical results for temperature (K). Lines indicate analytic solutions and symbols indicate results from flowfield computations. Figure labels correspond to streamlines in Figure 20: (a) streamline a, (b) streamline b, (c) streamline c.
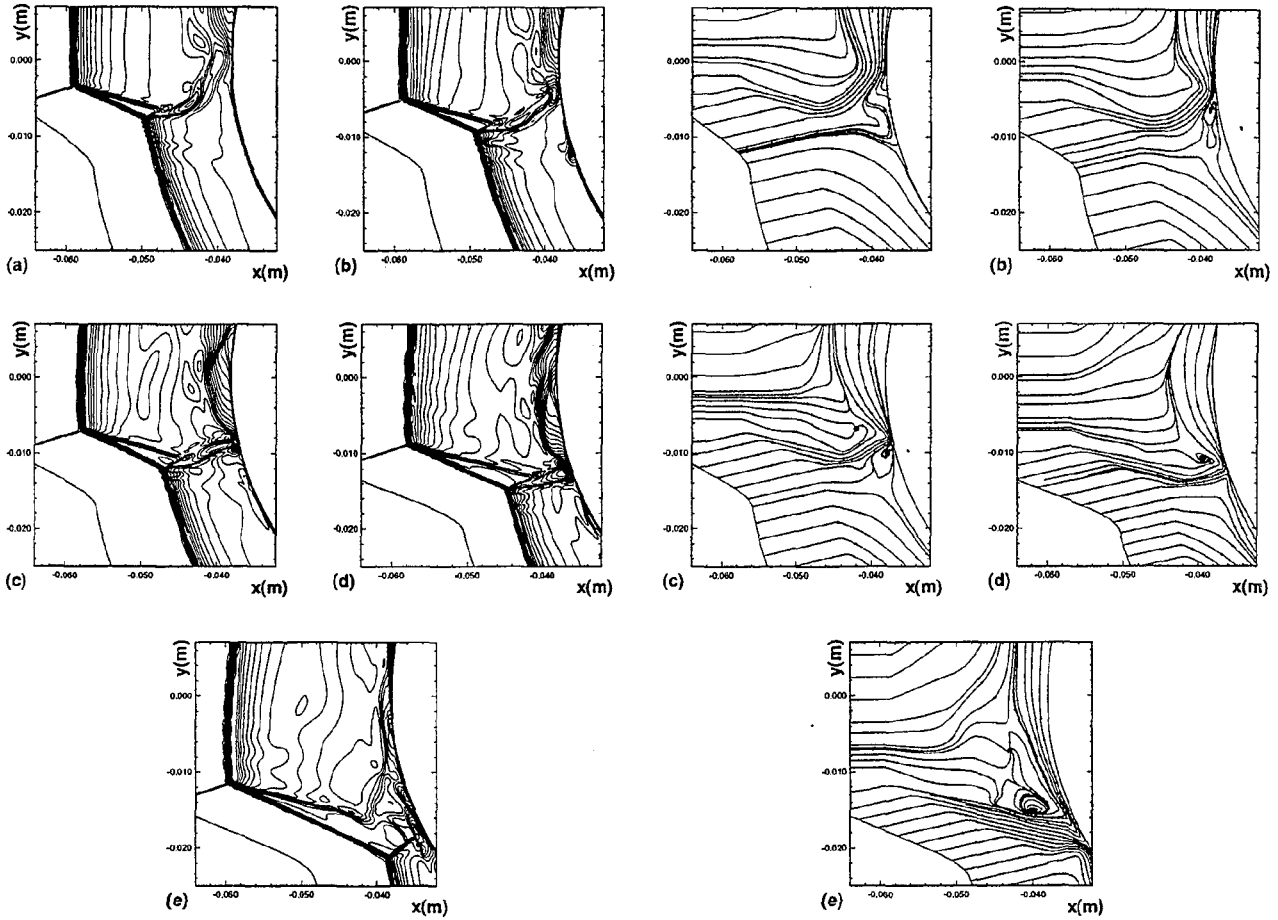
20
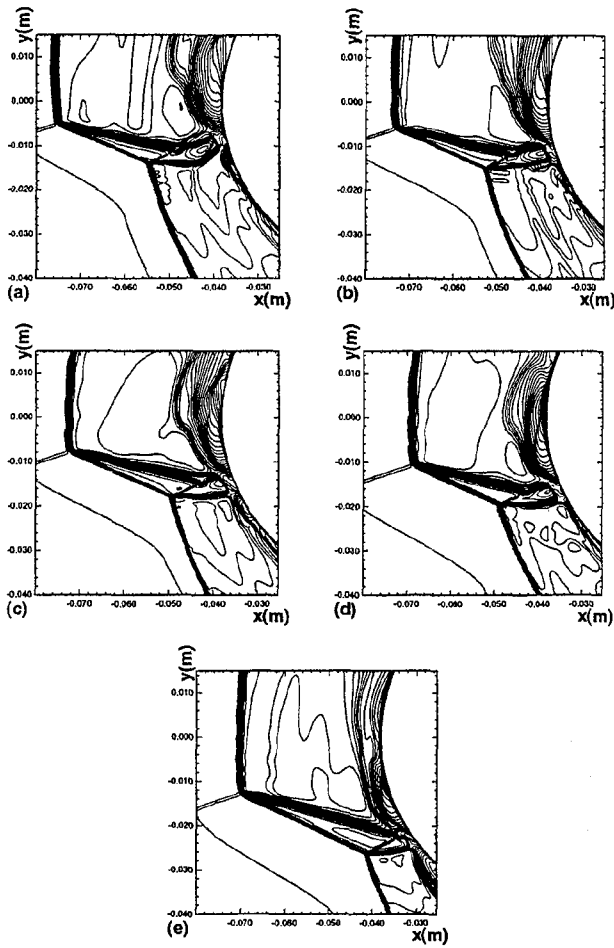
Figure 23: Instantaneous temperature contours showing the effect of shock impinging location for the perfect gas cases. (a) Case PG-1 ($\theta_{imp} = -4.16°$) (b) Case PG-2 ($\theta_{imp} = -4.65°$) (c) Case PG-3 ($\theta_{imp} = -6.19°$) (d) Case PG-4 ($\theta_{imp} = -8.94°$) (e) Case PG-5 ($\theta_{imp} = -10.5°$).
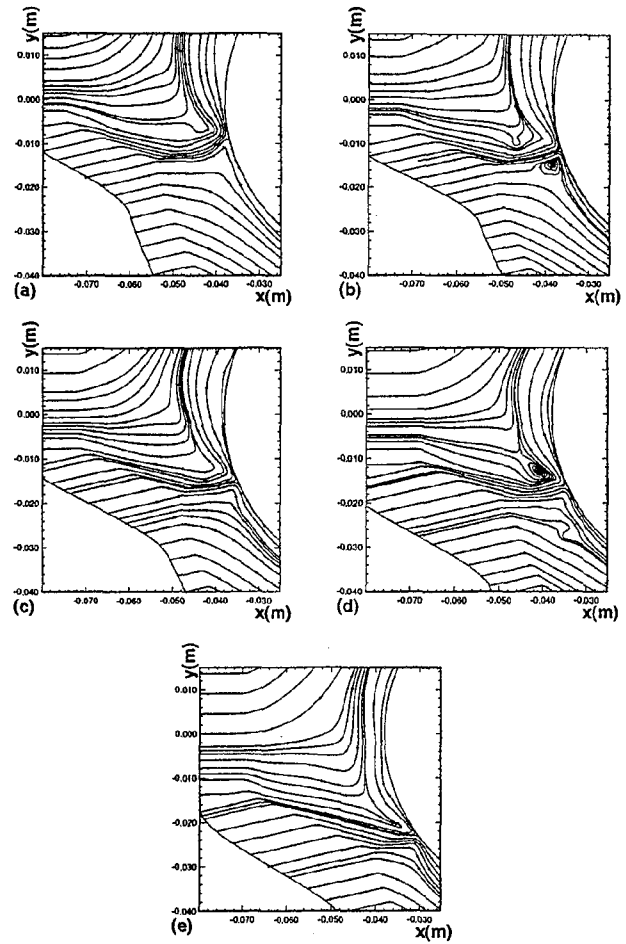
Figure 24: Instantaneous stream traces showing the effect of shock impinging location for the perfect gas cases. (a) Case PG-1 ($\theta_{imp} = -4.16°$) (b) Case PG-2 ($\theta_{imp} = -4.65°$) (c) Case PG-3 ($\theta_{imp} = -6.19°$) (d) Case PG-4 ($\theta_{imp} = -8.94°$) (e) Case PG-5 ($\theta_{imp} = -10.5°$).
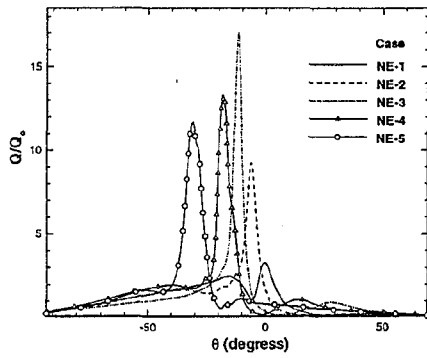
21
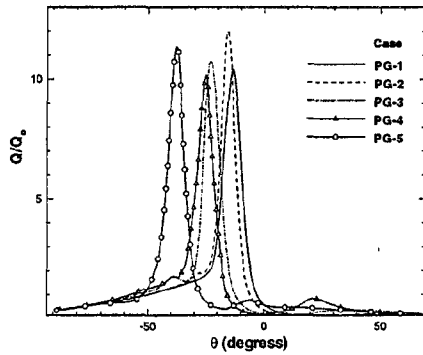
Figure 25: Normalized surface heat transfer profiles for the five different shock locations using the perfect gas model. Q_o is the undisturbed stagnation point heat transfer for a perfect gas.
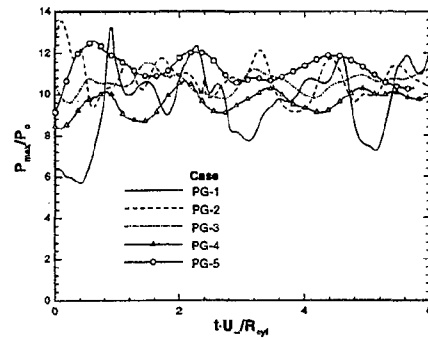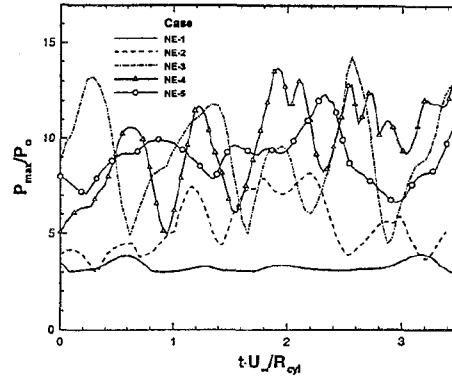

Figure 27: Time histories of normalized maximum surface pressure for the five different shock locations using the perfect gas model. P_o is the undisturbed stagnation point pressure for a nonequilibrium gas. Nondimensional time is given by tU_∞/R_{cyl}.
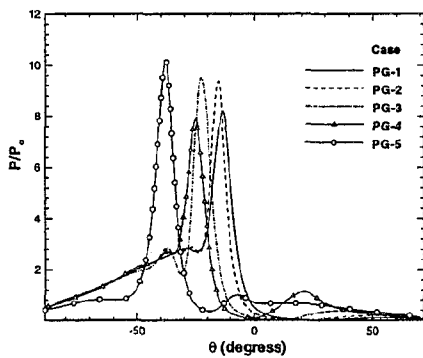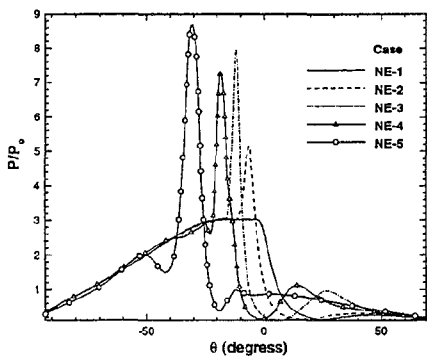

Figure 26: Normalized surface pressure profiles for the five different shock locations using the perfect gas model. P_o is the undisturbed stagnation point pressure for a perfect gas.

22

Figure 28: Instantaneous temperature contours showing the effect of shock impinging location for the nonequilibrium cases. (a) Case NE-1 ($\theta_{imp} = -3.19°$) (b) Case NE-2 ($\theta_{imp} = -4.84°$) (c) Case NE-3 ($\theta_{imp} = -6.94°$) (d) Case NE-4 ($\theta_{imp} = -8.83°$) (e) Case NE-5 ($\theta_{imp} = -11.2°$).

Figure 29: Instantaneous stream traces showing the effect of shock impinging location for the nonequilibrium cases. (a) Case NE-1 ($\theta_{imp} = -3.19°$) (b) Case NE-2 ($\theta_{imp} = -4.84°$) (c) Case NE-3 ($\theta_{imp} = -6.94°$) (d) Case NE-4 ($\theta_{imp} = -8.83°$) (e) Case NE-5 ($\theta_{imp} = -11.2°$).

23

Figure 30: Normalized surface heat transfer profiles for the five different shock locations using the nonequilibrium model. Q_o is the undisturbed stagnation point heat transfer for a nonequilibrium gas.

Figure 32: Time histories of normalized maximum surface pressure for the five different shock locations using the nonequilibrium model. P_o is the undisturbed stagnation point pressure for a nonequilibrium gas. Nondimensional time is given by tU_∞/R_{cyl}.
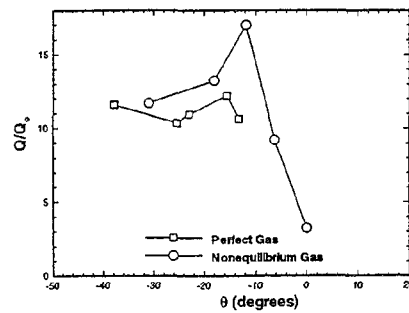

Figure 31: Normalized surface pressure profiles for the five different shock locations using the nonequilibrium model. P_o is the undisturbed stagnation point pressure for a nonequilibrium gas.

Figure 33: Time averaged peak surface heating normalized by undisturbed stagnation heating rate for different impinging shock locations and for both the nonequilibrium and perfect gas models.

24
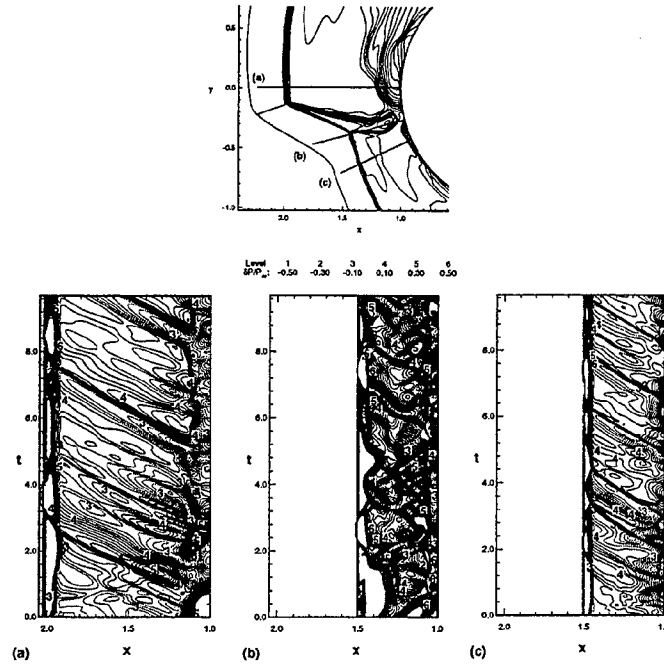
Figure 34: $x - t$ normalized pressure disturbance $(\delta p/p_{av})$ diagrams for perfect gas case PG-1. The upper figure denotes the radial lines along which the $x - t$ diagrams were taken in the lower figures.
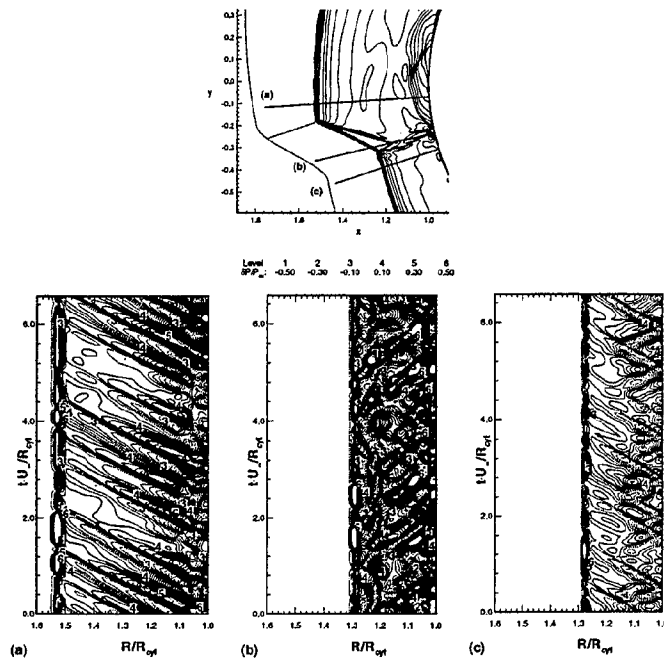

Figure 35: $x - t$ normalized pressure disturbance $(\delta p/p_{av})$ diagrams for nonequilibrium gas case NE-3. The upper figure denotes the radial lines along which the $x - t$ diagrams were taken in the lower figures.
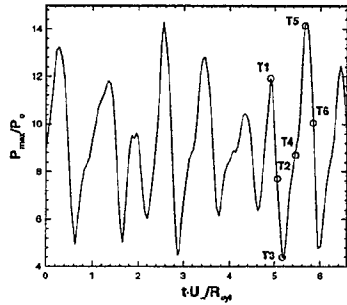
25

American Institute of Aeronautics and Astronautics

Figure 36: Normalized maximum surface pressure time history for type IV interaction for case NE-3.
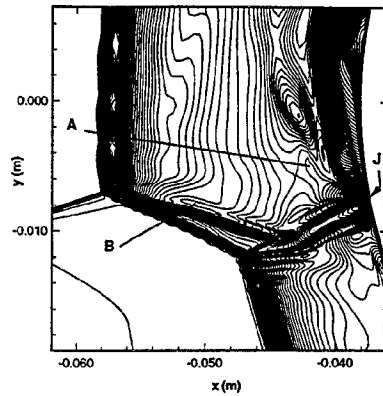
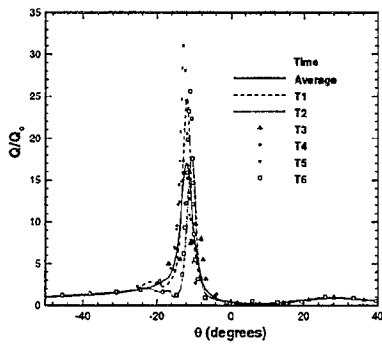Figure 39: Translational temperature contours for case NE-3 at time T1.

Figure 37: Surface heat transfer profiles normalized by undisturbed stagnation point heating rate for case NE-3. Time labels refer to labels in Figure 36.
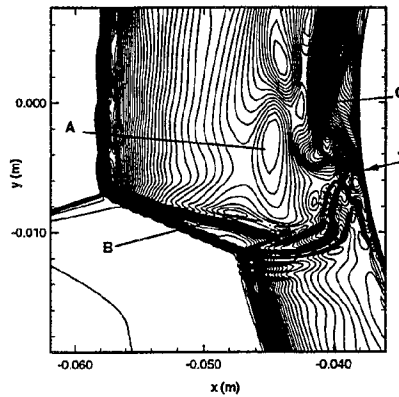

Figure 40: Translational temperature contours for case NE-3 at time T3.
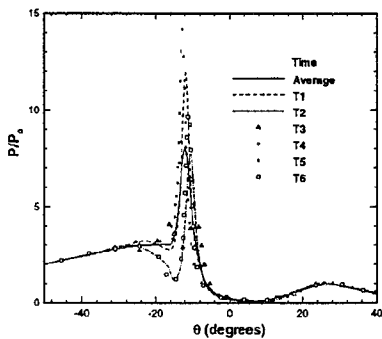

Figure 38: Surface pressure normalized by undisturbed stagnation point pressure for case NE-3. Time labels refer to labels in Figure 36.
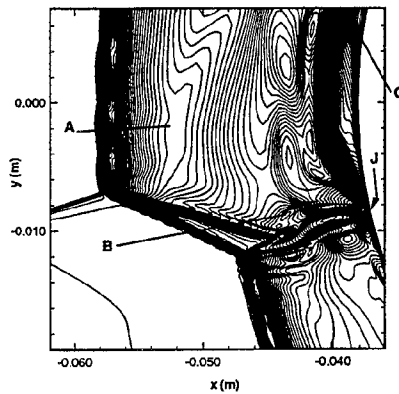

Figure 41: Translational temperature contours for case NE-3 at time T5.

26